ELSEVIER

International Journal of Heat and Fluid Flow 22 (2001) 39–52

International Journal of HEAT AND FLUID FLOW

www.elsevier.com/locate/ijhff

Spectral features of the wall-pressure fluctuations in turbulent wall flows with and without perturbations using LES

Stephane Viazzo [1], Anne Dejoan, Roland Schiestel *

Institut de Recherche sur les Phénomènes Hors Equilibre, I.R.P.H.E., U.M.R. 6594 CNRS/Universités d'Aix-Marseille I & II, 38 rue Frédéric Joliot Curie, 13451 Marseille Cedex 20, France

Received 14 October 1999; accepted 8 October 2000

Abstract

The statistical properties of the fluctuating wall-pressure field are studied using a numerical database generated by large eddy simulation of incompressible turbulent flow in a plane channel ($Re_\tau = 640$). Emphasis is given on the study of spectral features in the wavevector space and as a function of frequency, particularly in the region of low wavenumbers that are of major concern in submarine applications. A correction procedure is used to cancel the artificial pseudo-acoustic effect due to periodic boundary conditions. The influence of superimposed perturbations on one wall of the channel is considered afterwards in comparison with the non-perturbed case.

Keywords: Large eddy simulation; Wall-pressure field; Turbulence

1. Introduction

The knowledge of the wall-pressure fluctuations features beneath a turbulent boundary layer is of primary interest in many applications involving flow-induced vibration and sound generation. To this purpose, theories and models assume an accurate determination of the excitation source characterised by the spectral density in frequency and wavenumber. Indeed, the energy that the wall-pressure field can transmit to the solid body depends not only on the intensity of pressure forces but also on the relative scales in space and time of the exciting field. The study of the wall-pressure field, considering its numerous implications, has been examined over many years. In particular, the turbulent boundary layers on a flat plate have received extensive analytical and experimental investigations. A comprehensive summary of the theories linking the wall-pressure field to the physical structure of the turbulent boundary layer has been given by Blake (1986).

One of the major aspects of the wavenumber and frequency wall-pressure spectrum is the existence of a peak located at $k_x = \omega/U_c$ due to the convective properties of turbulence (ω is the frequency and U_c is the convective velocity). Its general shape is displayed in Fig. 1.

However, accurate measurements of wall-pressure fluctuations are not easy because of the probe sensitivity and the size of the transducers as well as the existence of a wide range of scales in the pressure fluctuations. In general, complete spectral data on the wall-pressure field necessary for the determination of flow-induced vibration and sound are not available from experiments. Numerical simulations are an appealing way to serve as a remedy for this lack of data.

In submarine acoustical problems where the flow is characterised by a low Mach number, the response of the system exhibits a resonance peak for wavenumbers clearly smaller than those of the highly energetic convective region. Although the energy associated with the low wavenumbers is negligible compared to the energy of the convective region, propagating velocities of the low wavenumber pressure sources are close to the perturbation velocities in the material, and thus they are able to produce a coupling with the modes of this solid material. This shows the importance of a detailed knowledge of wall excitation at low wavenumbers, because this range is mainly responsible for the excitations of solid structures immersed in a heavy fluid like water. Consequently, it is essential to determine the wall excitation for the low wavenumber range through its frequency and wavenumber spectra. In the low wavenumber region, measurements of the wall-pressure field are contaminated and blurred by noise due to the measuring devices. In this region, some of the theoretical models even seem to be contradicted by experiments. Indeed, Kraichnan (1956a,b) and Phillips (1956) indicate that the spectrum should vanish at long wavelengths following a $(k_x\delta)^2$ behaviour. Some semi-analytical models have been developed subsequently (Corcos, 1963; Chase, 1980, 1987; Witting, 1986; etc.) in order to give a better representation of the behaviour observed in experiments, and then the spectrum goes to a constant at large wavelengths. Nevertheless, the measurements and the different

* Corresponding author. Tel.: +33-0491118500; fax: +33-0491118502.
E-mail address: schieste@irphe.univ-mrs.fr (R. Schiestel).
[1] Present address: Département Systèmes Energétiques et Environnement, Ecole des Mines de Nantes, 4, rue Alfred Kastler, 44307 Nantes Cedex, France.

0142-727X/01/$ - see front matter
PII: S0142-727X(00)00074-6

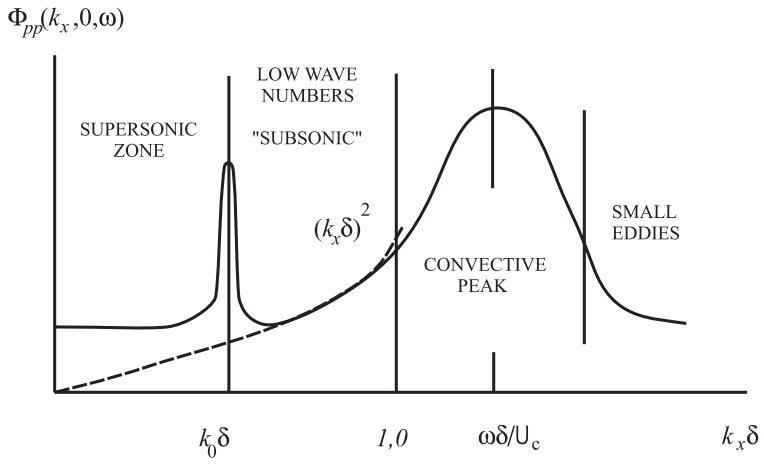

Fig. 1. General shape of the frequency and wavenumber wall-pressure spectrum.

models can present discrepancies reaching up to 40 dB in the low wavenumber range.

With the development of supercomputers, the numerical simulation of turbulent flows can now constitute a new efficient approach, which is complementary to both the experiments and theories in the study of the wall-pressure fluctuations. The wall-pressure field generated by direct numerical simulations of turbulent channel flow has been investigated by Kim (1989) and Choi and Moin (1990). The latter authors have computed the complete wavenumber and frequency spectra for a very moderate Reynolds number $Re_\tau = 180$. However, at such a Reynolds number, the low wavenumber zone and the convective zone are not dissociated enough to allow the determination of the different scaling behaviours reported by experiments and by theoretical models (also, often calibrated on the experiments). In contrast, the large eddy simulations are not limited to low Reynolds numbers, since by a spectral partition only the large energetic scales are computed while the more universal fine scales are modelled (without the very fine grid needed in DNS).

The main goal of the present paper is to examine the wall-pressure field generated by large eddy simulation with a particular focus on its spectral features in the low wavenumber range that are of practical interest for many applications related to acoustical problems. The present wall-pressure database is provided by the large eddy simulation code (SET-HF2) developed by Schiestel and Viazzo (1995) for the channel flow. One of the purposes of the present study is to deliver a description, as complete as possible, of the wavenumber and frequency spectrum of the wall-pressure fluctuations, and especially in the low wavenumber range. In a second step, the influence of space-time periodic perturbations which are superimposed at the lower wall of the channel is considered in order to appreciate to what extent the pressure spectrum distributions are modified or not. The approach considers only the effect of a periodic normal wall velocity of small amplitude.

2. Numerical approach and methodology

The basic idea of large eddy simulation is that the large-scale motions differ strongly from one flow to another and are directly affected by the boundary conditions, whereas smaller eddies have a more universal behaviour. The large anisotropic turbulent structures are difficult to model since they have large space-time characteristic lengths. The fine scales are easier to describe even with relatively rough models provided their dissipative nature is taken into account, since they are assumed to be universal. The large eddy simulation method consists in resolving explicitly the time-dependent and three-dimensional motions of large scales, while the influence of the discarded smaller subgrid scales must be modelled appropriately.

2.1. Computational domain and its characteristics

The geometry of the flow and its coordinate system are sketched in Fig. 2. From a statistical point of view, the fully turbulent channel flow is homogeneous in the streamwise (Ox) and spanwise (Oy) directions. Consequently, periodic boundary conditions are appropriate in these two directions. Such boundary conditions are justified only if the computational domain (its period) is large enough to account for the larger turbulent structures of the flow. On the basis of experimental two-point correlations by Comte-Bellot (1963), dimensions of the computational domain are adjusted in such a way that the fluctuations are practically decorrelated on half a period in these directions. The measurements by Comte-Bellot indicate that the decorrelation occurs for a space separation of 3.2δ and 1.6δ, respectively, in the streamwise and spanwise directions (where δ is the half-width of the channel).

For the applications under consideration (description of the low wavenumber range), the dimension in the streamwise direction is prescribed larger in order to reach long wavelengths. Thus, we choose the following dimensions of the computational box: $L_x = 6\pi\delta$; $L_y = 3\pi\delta/2$; $L_z = 2\delta$. Also, in the very near wall region, the larger structures called streaks play an important part in the production process of turbulence. It is essential to compute as well as possible these streaky structures which have a mean spacing of $\lambda^+ = 100$ at $z^+ = 5$, and up to

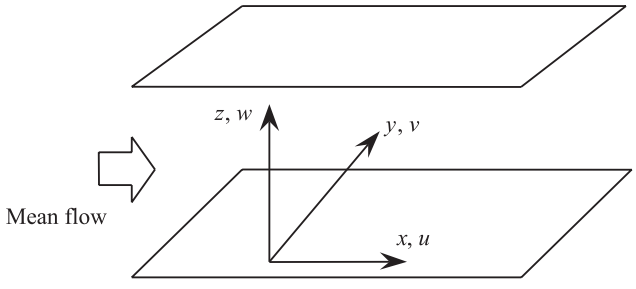

Fig. 2. Sketch of the plane channel flow and definition of coordinates.

$\lambda^+ = 150$ at $z^+ = 35$ in wall coordinates along the spanwise direction. In the non-homogeneous direction (Oz) normal to the walls, the grid is non-uniform with a strong refinement near the walls using the following hyperbolic transformation:

$$z = \frac{1}{a}\tanh[Z\tanh^{-1}(a)], \tag{1}$$

where Z is the uniform coordinate in the transformed space and a is an adjustable parameter controlling the refinement. By choosing $N_z = 62$ grid points in the (Oz) direction and $a = 0.98346$, this gives three grid points in the viscous layer ($z^+ < 5$). The computations are carried out with 4,571,136 grid points (i.e. $384 \times 192 \times 62$ in the x, y and z directions, respectively) for a Reynolds number Re_τ equal to 640 based on the wall shear velocity u_τ and the half-width δ of the channel. Table 1 shows the general grid characteristics (the superscript "+" indicates the wall units).

In Figs. 3 and 4, the two-point correlations and the one-dimensional spectra of the velocity fluctuations are reported. Both the correlations and the spectra are displayed for two distances from the lower wall $z^+ = 15$ (location of the maximum of the turbulent kinetic energy) and $z^+ = 640$ (centre of the channel). All the one-dimensional spectra are normalised to verify:

$$\begin{aligned}\overline{u'^2} &= \int_0^\infty E_{uu}(k_x)\,\mathrm{d}k_x,\\ \overline{v'^2} &= \int_0^\infty E_{vv}(k_x)\,\mathrm{d}k_x,\\ \overline{w'^2} &= \int_0^\infty E_{ww}(k_x)\,\mathrm{d}k_x,\end{aligned} \tag{2}$$

here the overbar indicates averaging.

These results demonstrate the adequacy of the computational domain and its grid resolution since the two-point correlations vanish for large separation distances and the energy density associated with high wavenumbers is several decades below the energy density of low wavenumbers. Note that the inertial range following a $k_x^{-5/3}$ law is very limited due to the effective filtering and also due to the effect of the relatively moderate Reynolds number ($Re_\tau = 640$).

2.2. Fundamental equations, subgrid scale modelling and numerical aspects

In large eddy simulations, each variable f of the flow is split into a large-scale component $\bar{f}$ and a residual component f' called the subgrid scale component, by using a filtering operator. Dynamical equations of the large-scale flow field, obtained by filtering the Navier–Stokes equations, are written as the following system:

$$\begin{aligned}\frac{\partial \bar{u}_i}{\partial t} &= F_i - \frac{\partial \bar{P}}{\partial x_i} + H_i - \frac{\partial \tau_{ij}}{\partial x_j} + \frac{1}{Re_\tau}\nabla^2 \bar{u}_i,\\ \frac{\partial \bar{u}_i}{\partial x_i} &= 0,\end{aligned} \tag{3}$$

in which Re_τ denotes the Reynolds number defined as $Re_\tau = u_\tau \delta/\nu$, H_i contains the non-linear terms, $F_i = d_{i1}$ the mean gross pressure gradient necessary to maintain the motion and τ_{ij} is the subgrid scale stress tensor. The pressure $\bar{P}$ is referred to as the "pseudo-pressure" because it includes the spherical part of the subgrid scale stress tensor. Note that this pseudo-pressure on the walls is equal to the actual wall

Table 1
Characteristics of the computational domain

N_x	N_y	N_z	L_x	L_y	L_z	h_x/δ	h_y/δ	h_z/δ	h_x^+	h_y^+	h_z^+
384	192	62	$6\pi\delta$	$3\pi\delta/2$	2δ	0.049	0.025	1.38×10^{-3}–8.1×10^{-2}	31.4	15.71	0.88–51.84

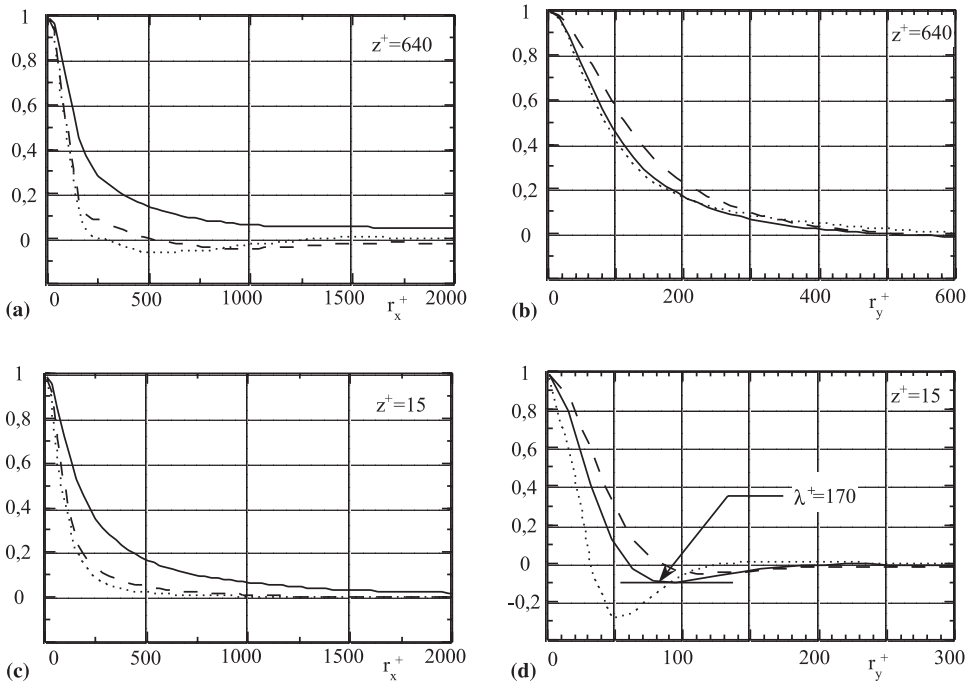

Fig. 3. Two-point velocity correlations for two locations from the wall. — R_{uu}, -- R_{vv}, ··· R_{ww}, (a) and (c): longitudinal; (b) and (d): transverse.

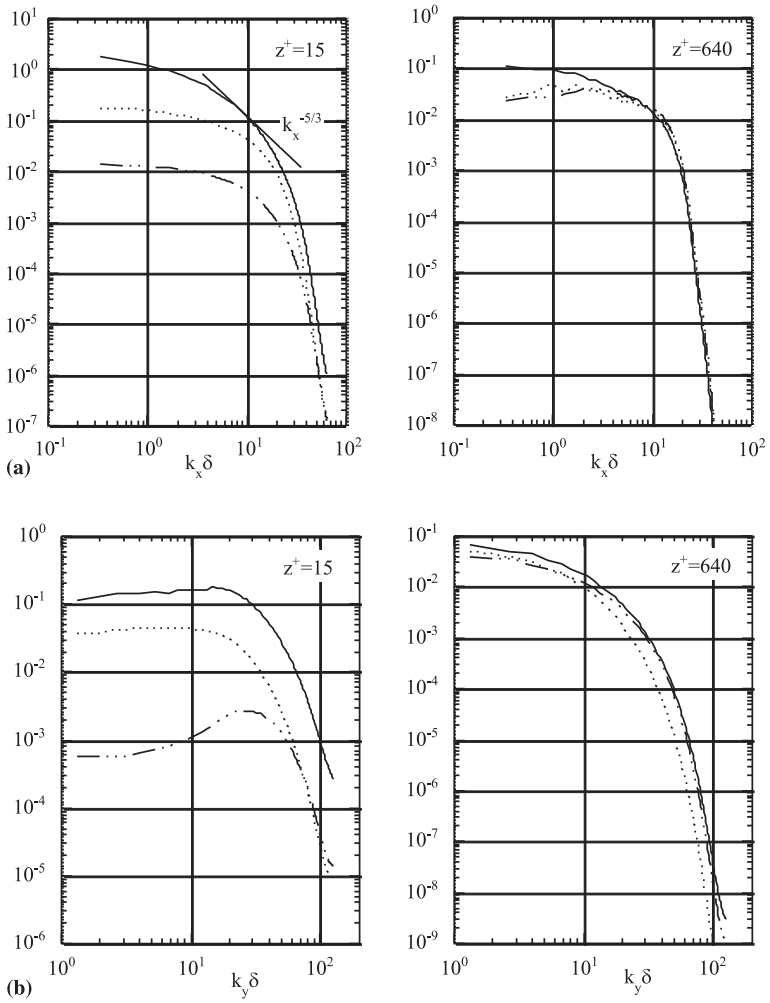

Fig. 4. One-dimensional velocity spectra — E_{uu}, – · · – E_{vv}, · · · E_{ww}, (a) longitudinal; (b) transverse.

pressure due to no-slip boundary conditions which entail zero SGS stresses.

Here, all the quantities are non-dimensionalized using the wall shear velocity u_τ and the half-width δ of the channel.

The numerical method (cf. Schiestel and Viazzo, 1995) is based on the Hermitian finite differences in the inhomogeneous (Oz) direction and Fourier pseudo-spectral representation in the homogeneous (Ox) and (Oy) directions in a staggered arrangement. The time integration uses a hybrid Adams–Bashforth and Crank–Nicolson scheme. The accuracy of the algorithm has been tested previously (Viazzo and Schiestel, 1995) by comparisons with hydrodynamic stability results.

The subgrid scale terms are formally identical to the Reynolds stresses, but have a somewhat different significance. The subgrid scale terms express complex interactions between the resolved and unresolved scales, thereby reflecting some local and non-local interactions. Most subgrid scale models are based on the eddy viscosity expressed either in the physical space or in the spectral space. Because the pseudo-spectral algorithm used in the present code is developed in physical space, we retain an eddy viscosity model in the physical space. A simple justification of the choice of an eddy viscosity model which relies on an analogy with molecular viscosity is that the channel flow considered here is not far from equilibrium. Indeed, the major role of finer scales is to dissipate the energy coming from the larger ones through energetic transfer cascade, at least for turbulent flows with simple geometric configurations near an equilibrium state.

The system of equations (3) is closed using a variant of the Smagorinsky model, that is the two-part model of Schumann (1975) used also by Moin and Kim (1982). This model consists in splitting the subgrid scale stress tensor into two parts, one is locally isotropic and the other one is non-homogeneous, then it reads as follows:

$$\tau_{ij} = -2\nu_t(\bar{S}_{ij} - \langle\bar{S}_{ij}\rangle) - 2\nu_t^*\langle\bar{S}_{ij}\rangle, \tag{4}$$

where $\bar{S}_{ij}$ is the strain tensor and $\langle\cdot\rangle$ denotes a space averaging over homogeneous planes. The second part takes into account explicitly for the contribution of the mean shear stress $\partial\bar{U}/\partial z$ whereas the first one plays an essentially dissipative role.

The eddy viscosity ν_t in the homogeneous Smagorinsky part is written as

$$\nu_t = (C_S l)^2\sqrt{2(\bar{S}_{ij} - \langle\bar{S}_{ij}\rangle)(\bar{S}_{ij} - \langle\bar{S}_{ij}\rangle)}, \tag{5}$$

where l is a length characteristic of the larger subgrid scales damped by a Van Driest corrective factor to consider the action of viscosity in the vicinity of the walls:

$$l = [1 - \exp(-z^+/A^+)](\Delta_1\Delta_2\Delta_3)^{1/3} \tag{6}$$

with $A^+ = 25$ and $C_S = 0.065$.

The eddy viscosity ν_t^* is also damped by a corrective factor:

$$\nu_t^* = c(D\Delta_2)^2\sqrt{2\langle\bar{S}_{ij}\rangle\langle\bar{S}_{ij}\rangle}, \tag{7}$$

where

$$D = 1 - \exp(-z^{+2}/A^{+2}) \quad \text{with } c = 0.05. \tag{8}$$

In the latter expression, the characteristic length scale is the filter width Δ_2 in the spanwise direction since, near the walls, the most important structures are the streaky structures finely spaced in the spanwise direction and only present very near the walls.

In the present case, the filtering is explicit over homogeneous planes parallel to the walls, whereas in the (Oz) direction the filtering is implicitly induced by the finite difference scheme. Based on a pseudo-spectral algorithm (finite differences and Fourier expansions), the present computations use a Gaussian filter which produces a progressive and smooth transition between resolved and unresolved scales. Generally, the filter width Δ_i is chosen twice the mesh spacing h_i in the direction i (cf. Kwak et al., 1975).

It is very difficult to determine accurately the cut-off wavenumbers of filtering since the cut-off is progressive both in spectral and physical spaces in the streamwise and spanwise directions: the Gaussian filter indeed extends somewhat into the large-scale range. In the normal direction to the walls, it is particularly not easy to specify the characteristics of the filter implicitly induced by the finite differences. The overall cut-off wavenumber can be estimated by considering the $-5/3$ slope of the inertial range expected at sufficiently high Reynolds numbers. Indeed, the one-dimensional velocity spectra reported in Fig. 4 indicate that the filtering responsible for the pronounced narrowing of the inertial range occurs nearly at $k_{xc}\delta = 12$. Also, this value can be compared by superimposing the present one-dimensional spectra to the other ones provided by a previous simulation carried out with $64 \times 96 \times 62$ grid points and a smaller computational box with $L_x = 4\pi\delta$, $L_y = \pi\delta$ and $L_z = 2\delta$ (cf. Viazzo, 1993). By superimposing the two curves, the cut-off wavenumber of the coarse mesh can be estimated at $k_{xc}\delta = 3$. Using the Gaussian filter function in spectral space $F = \exp\left[-k_{xc}^2\Delta_x^2/24\right]$ and assuming similarity (this is justified only because the numerical scheme and the subgrid model remain identical), the quantities F and $k_{xc}\Delta_x$ remain constant. Thus, the cut-off wavenumber of the present simulation is recovered, namely $k_{xc}\delta = 12$.

For convenience and without confusion with the filtering operator, the overbar $\overline{(\cdot)}$ will denote hereafter the average of the large-scale component over x, y and t, and the prime its perturbation from this value.

3. Wall-pressure fluctuations in the non-perturbed case

3.1. Computational technique of the wavenumber and frequency spectrum

In the numerical simulations, it was pointed out by Choi and Moin (1990) that the growth of a secondary peak in the frequency and wavenumber spectra located at the smallest computational wavenumber permitted by the computational box size. In experimental facilities, the presence of such a peak would be attributed to acoustic effects. But, both in these DNS and in the present LES computations, no acoustic effect is accounted for, since the simulations are performed using the incompressible Navier–Stokes equations. Choi and Moin attribute this phenomenon to the use of periodic boundary conditions (Fourier expansions along the homogenous directions) which are able to generate wave-like propagating perturbations by a feedback mechanism. It is interesting to notice that this peak always appears at the lowest wavenumber whatever the window type and the computational domain used. However, this artificial sound is negligible in terms of energy (it represents less than 1% of the root-mean-square of the pressure fluctuations), but its effects on the wavenumber and frequency spectrum are particularly undesirable in the low wavenumber range. These artificial acoustic contributions can also affect the scaling behaviour of the autospectrum in the low frequency region.

If these perturbations in LES calculations are associated with the artificial acoustic, they can be considered as plane waves propagating along the streamwise direction. So it is judicious to use a classical cancellation technique like in experiments. Generally, the procedures of noise cancellation are based on the subtraction of two (or three) spanwise signals in order to obtain non-contaminated wall-pressure fluctuations (Simpson et al., 1987; Bally, 1989). In the present technique, we prefer to use the subtraction of the two pressure fields on the lower and upper walls. Indeed, this practice allows to use the complete available database, and avoids to reduce the spanwise periodicity. The spectral densities are calculated using standard techniques for the random process of a stationary function. The total time of integration of the pressure fields on both walls is divided into m overlapping intervals in which the pressure is weighted by a window function. In the jth interval, the modified pressure is

$$\tilde{p}^{(j)}(x, y, \pm\delta, t) = p^{(j)}(x, y, \pm\delta, t)g(t), \tag{9}$$

where g is here the Hanning window (see Viazzo, 1993).

The turbulent power spectrum is thus obtained by subtraction of the two signals of pressure on the lower and upper walls, namely:

$$\tilde{\phi}^{(j)}(k_x, k_y, \omega) = \frac{1}{2}\hat{f}^{(j)}(k_x, k_y, \omega)\hat{f}^{(j)*}(k_x, k_y, \omega), \tag{10}$$

where $\hat{f}^{(j)}(k_x, k_y, \omega)$ is the Fourier transform in the x-direction, y-direction, and time of the difference: $\tilde{p}^{(j)}(x, y, +\delta, t) - \tilde{p}^{(j)}(x, y, -\delta, t)$ (the asterisk denotes the complex conjugate).

The expression (10) is valid because the two pure turbulent fields and the pseudo-acoustic part are uncorrelated. In the present computations, the mean square of the two pure turbulent fields is negligible (about 10^{-2}) with respect to the mean square of the pressure on each wall (nearly equal to 3.5). The pseudo-acoustic and the pure turbulent parts are assumed to be uncorrelated because the artificial acoustic part is only connected with the numerical method and so it is not linked to any physical phenomenon.

The frequency and wavenumber spectrum is thus obtained by the following ensemble average over the m overlapping intervals:

$$\phi(k_x, k_y, \omega) = \frac{1}{m}\sum_{j=1}^{m}\tilde{\phi}^{(j)}(k_x, k_y, \omega). \tag{11}$$

The two-dimensional and the one-dimensional spectra are computed by summing $\phi(k_x, k_y, \omega)$ over the remaining variables, for instance:

$$\phi(k_x, \omega) = \int_{-\infty}^{+\infty}\phi(k_x, k_y, \omega)\,\mathrm{d}k_y. \tag{12}$$

Due to the use of a window function, the integral over $\phi(\omega)$ is generally not equal to the mean square of the wall-pressure. So, in order to recover this important property, all the spectra are rescaled. The two-point correlations are obtained by inverse Fourier transform of the spectrum. The mean square of pressure fluctuations $\overline{p'^2}$ is then defined by

$$\overline{p'^2} = \int_0^{+\infty} \phi(\omega)\,\mathrm{d}\omega. \tag{13}$$

Once the statistical steady state is reached, the filtered Navier–Stokes equations are integrated over 22,400 time steps and the pressure on both the walls is stored in every ten time steps ($\Delta t' u_\tau/\delta = 4 \times 10^{-3}$). The total time of storage corresponds to a value of $8.96\delta/u_\tau$ with $N = 2240$ samples, and it is divided into $m = 13$ overlapping intervals, each containing $M = 320$ samples. The frequency range is $0 \leqslant \omega \leqslant 785.4u_\tau/\delta$ with the frequency resolution $\Delta\omega = 4.91u_\tau/\delta$. The wavenumber ranges are, respectively, in the streamwise and in the spanwise directions $0 \leqslant k_x\delta \leqslant 64.4$ and $0 \leqslant k_y\delta \leqslant 128$ with the wavenumber resolutions $\Delta k_x\delta = 0.333$ and $\Delta k_y\delta = 1.333$. The estimated cut-off frequency is $\omega_c\delta/u_\tau = 141$ using the Taylor hypothesis with $U_c = 0.65U_0$ and the cut-off wavenumber $k_{xc}\delta = 12$.

3.2. One point statistics

Figs. 5–7 show the numerical results for the rms pressure fluctuations normalised by the shear velocity and the half-width of the channel, and the results for the skewness and the flatness factors versus the distance to the wall. The rms of the pressure fluctuations reaches a maximum value of about 2 at the vertical location $z^+ = 37$ and approximately 1.85 at the wall. This value is somewhat lower than the one given by the experimental data in boundary layers for which a value lying between 2 and 3 is usually obtained. The remarks in the previous paragraphs can give a plausible explanation of this result. Higher order statistics appear to be much more sensitive to spatial and temporal resolutions and to the integration interval for statistical averaging. This is revealed by small residual oscillations and asymmetries still visible in Figs. 6 and 7. The limiting value at the wall of the flatness factor is 4.2 while the value reported by Schewe (1983) is equal to 4.9 for the smallest of the transducers. However, Schewe finds a continuous decay of the flatness factor when size of the transducers is increasing. It could be understood that the filtering induced by the LES method is acting in a similar way and then yields a lower value of variance. Schewe also obtained a negative value for the skewness factor at the wall for the smallest transducers while it is positive for the largest one. According to this result, filtering in the present LES calculation may produce the same trends: this may explain why we obtain a positive value in the present computations by using filtering. Also, the DNS results of Kim (1989) in which no filtering is used accordingly gave a negative value. Across the whole channel, the skewness and flatness factors of the pressure fluctuations differ significantly from the Gaussian distribution (0 and 3, respectively). This reveals the intermittent behaviour of pressure fluctuations that appear quite pronounced.

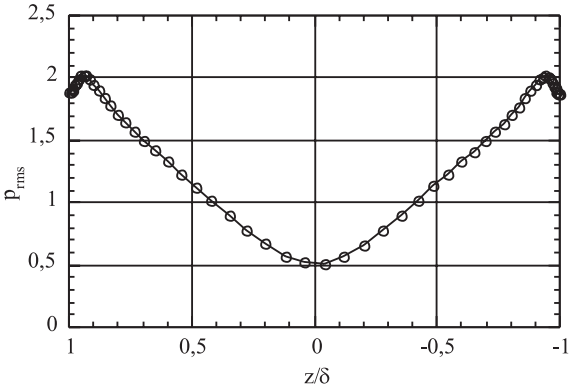

Fig. 5. Normalised rms pressure.

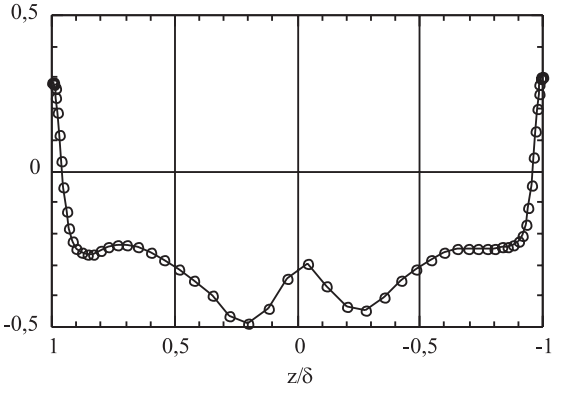

Fig. 6. Skewness factor of the pressure fluctuations.

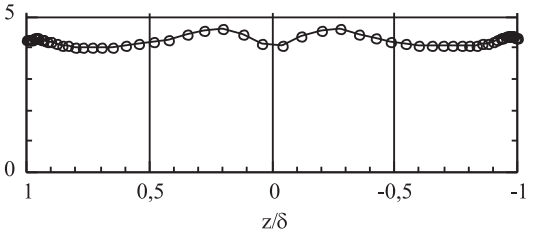

Fig. 7. Flatness factor of the pressure fluctuations.

3.3. Spectral features: one-dimensional spectra

In turbulent boundary layers, it is rather well established that the autospectrum $\phi(\omega)$ includes three distinct spectral regions as well as an intermediate one strongly dependent on the Reynolds number. In the very low-frequency range (say $\omega\delta/u_\tau \leqslant 5$), the spectrum follows a ω^2 behaviour (cf. Bradshaw, 1967; Panton et al., 1980) as far as the noise cancellation techniques are used. According to Farabee and Casarella (1991), the experimental data collapse with the dynamic pressure $q = -\rho U_0^2/2$ and δ^*/U_0 scaling. At low frequency, say $5 \leqslant \omega\delta/u_\tau \leqslant 100$, the autospectrum collapses with the outer variable scaling τ_w, u_τ and δ with a $+0.4$ slope. The maximum value is reached for $\omega\delta/u_\tau \approx 50$. The third spectral region, the extent of which is strongly dependent on the Reynolds number, displays a -1 slope. Panton and Linebarger (1974) and Bradshaw (1967) have shown that the outer and inner variable scalings are both valid. Moreover, Panton et al. (1980) established that this region exists only if $Re_\tau \geqslant 333$. According to Farabee et al., the range of existence of this zone is $100 \leqslant \omega\delta/u_\tau \leqslant 0.3Re_\tau$, or $100/Re_\tau \leqslant \omega\nu/u_\tau^2 \leqslant 0.3$. In the very high-frequency range, another region with a -5 slope exists for $Re_\tau \leqslant \omega\delta/u_\tau$, collapsing with inner variable scaling. Note that for the frequency range $0.4Re_\tau \leqslant \omega\delta/u_\tau \leqslant Re_\tau$, Schewe (1983) observes a $-7/3$ slope previously predicted by Monin and Yaglom (1975).

The different scalings of this spectral distribution give some interesting insights into the location of the turbulent sources responsible for the various spectral wall-pressure mechanisms. The outer variable scaling suggests that the medium frequency range is due to the outer part of the boundary layer. We can expect that this region has a different behaviour in the case of

the channel flow, since in the outer region, structure of the turbulence is quite different from that in the boundary layer. In contrast, in the high-frequency range the inner variable scaling indicates that the eddy motions proceed from the turbulent activity inside the buffer zone. In the near wall region, structure of the turbulence in the channel flow and in the boundary layer are very similar: this corresponds to a -5 slope in both cases, which has been already found by the DNS calculations of Choi and Moin (1990). It has been argued that contribution of the turbulent activity in the logarithmic region to wall pressure leads to a -1 slope in the case of the turbulent boundary layer. We can also expect the same behaviour in the channel flow. Note that due to a very low Reynolds number $Re_\tau = 180$, the DNS of Choi and Moin in channel flow shows a negligible zone with -1 slope.

Practically, the artificial pseudo-acoustic contamination that occurs only in the very low-frequency range of the power autospectrum can be reduced using the noise cancellation technique. Despite the use of this noise cancellation technique, the behaviour in the very low-frequency range remains distinctly different from those in the boundary layer: the autospectrum does not vanish according to a ω^2 law, but seems to keep a constant level. As conjectured by many authors, the presence of such a plateau is linked to the particular structure of the fully turbulent channel flow: this confirms that the induced irrotational flow centred in the outer region is a contributor to the low-frequency range in turbulent boundary layers.

In Fig. 8 the frequency spectrum is normalised using the internal variables u_τ and ν. The existence of a ω^{-1} region is limited to a very narrow interval of frequencies ($100 \leqslant \omega\delta/u_\tau \leqslant 140$). The end of this zone roughly corresponds to the position of the cut-off wavenumber of the numerical simulation which is estimated to a value around $\omega_c\delta/u_\tau \approx 141$. It appears to be acceptable to model the frequency spectrum of the pressure field according to a zonal description as follows:

$0 \leqslant \omega\delta/u_\tau \leqslant 100$ – similarity region of the frequency spectrum;

$100 \leqslant \omega\delta/u_\tau \leqslant 0.4Re_\tau$ – frequency spectrum with ω^{-1} decay law;

$0.4Re_\tau \leqslant \omega\delta/u_\tau \leqslant Re_\tau$ – frequency spectrum with $\omega^{-7/3}$ decay law;

$Re_\tau \leqslant \omega\delta/u_\tau$ – frequency spectrum with ω^{-5} decay law.

The resulting calculated spectrum which includes the previous corrections is also given in Fig. 8. This practice allows to extrapolate the calculated spectrum through the high wavenumber zone where the filter of the simulation produces a steep decrease. It is then possible to find a relation giving the wall rms pressure in a plane channel as a function of the Reynolds number like in Panton and Linebarger (1974). For frequencies in the medium range of $0 \leqslant \omega\delta/u_\tau \leqslant 100$ in which no filtering effect is involved, numerical summation of the calculated spectrum gives $p^2_{\mathrm{rms}}/\tau^2_p = 1.914$. In the $100 \leqslant \omega\delta/u_\tau \leqslant 0.4Re_\tau$ zone with the hypothesis of a ω^{-1} law, the numerical summation gives $p^2_{\mathrm{rms}}/\tau^2_p = \mathrm{Ln}(Re_\tau/250)$, noting that this contribution exists only if $0.4Re_\tau \leqslant 100$. The energy associated with the $\omega^{-7/3}$ zone is independent of the Reynolds number and the numerical summation gives $p^2_{\mathrm{rms}}/\tau^2_p = 1.03$. The energetic contribution of the very high-frequency zone is negligible.

By adding these different contributions, the total variance can be expressed as

$$p^2_{\mathrm{rms}}/\tau^2_p = 3 + 2\,\mathrm{Ln}(Re_\tau/250). \tag{14}$$

This correlation is in good agreement with the data in a plane channel as seen in Fig. 15 which suggests that for a same Reynolds number, energy of the fluctuations of the wall pressure is higher in a boundary layer than in a plane channel. This can be explained by the spectral distribution in the medium frequency range which differs from a channel flow to a boundary layer: in particular the spectral level is lower. It is also worth noting that although this relation has been established for higher Reynolds numbers such that $Re_\tau \geqslant 250$, it still appears in good agreement with the DNS calculation of Choi and Moin (1990) for $Re_\tau = 180$. For Reynolds numbers lower than 250, the pressure spectrum in the medium frequency range does not reach a similarity behaviour and then $\mathrm{Ln}(Re_\tau/250) < 0$. Even if Eq. (14) remains valid at lower Reynolds numbers $Re_\tau \leqslant 250$, the pressure fluctuations exhibit a behaviour which is distinctly different from the one observed for the higher values above 250. It then looks hard to make extrapolation of the results obtained for Reynolds numbers lower than 250 to practical situations in which the Reynolds number is much higher. The LES method seems more suitable than the DNS in this case, for the determination of spectral properties of the wall-pressure field in real situations.

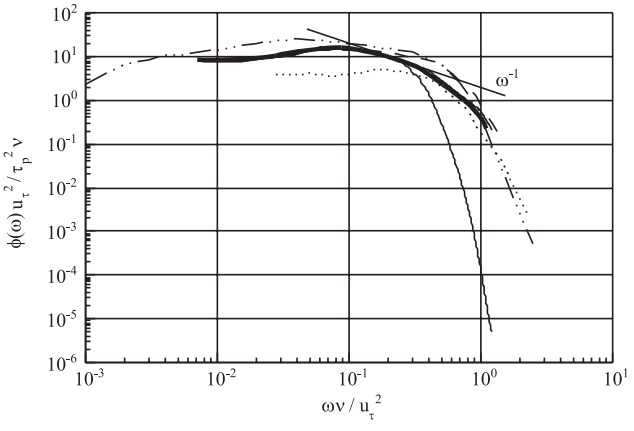

Fig. 8. Frequency spectra of the wall-pressure Present calculation: — without correction; ▬ with correction. ····· (Choi and Moin, 1990, DNS, $Re_\tau = 180$); – – – – – – (Schewe, 1983, exp.); —···—···—, (Farabee and Casarella, 1991, exp.).

3.4. Three-dimensional spectrum

Contour plots of the frequency-wavenumber pressure spectrum are shown in Fig. 9, clearly exhibit the well-known convective crest. Some noise is still visible on the contours because of the limited time interval of statistical treatment. The wavevector spectrum in the x, y directions given in Fig. 10 is also somewhat noisy but its general shape is entirely satisfactory.

Fig. 11 for the three-dimensional spectrum at low wavenumbers shows that a small artificial pseudo-acoustic peak develops because of the longitudinal periodicity condition. As we have commented before, this perturbation is however entirely negligible in energetic terms and limited to very small wavenumbers.

The three-dimensional spectrum in Fig. 12 shows that the convective peak has a non-symmetrical shape, a character that has been already remarked by several authors. This asymmetry progressively cancels at higher frequencies. It is also important to keep in mind the fact that the experimental results obtained by using wall-pressure transducers of finite diameter are necessarily underestimated because of the local averaging effect. This fact has to be taken into account when comparing between experiment and calculation.

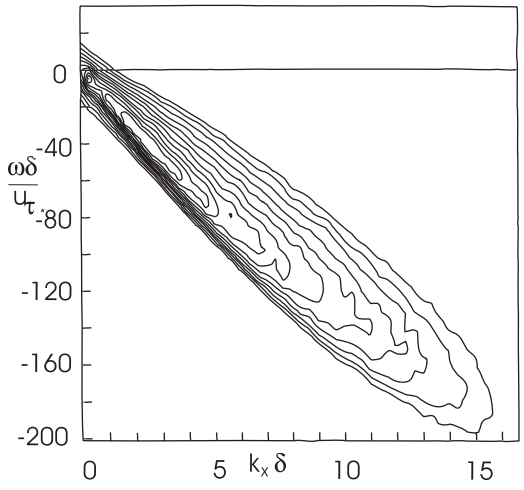

Fig. 9. Contour plots of the frequency and wavenumber spectrum of the wall-pressure fluctuations $\phi(k_x,\omega)u_\tau/\tau_p^2\delta^2$ plotted in dB (11 levels from -30 to -20 dB with 1 dB increment).

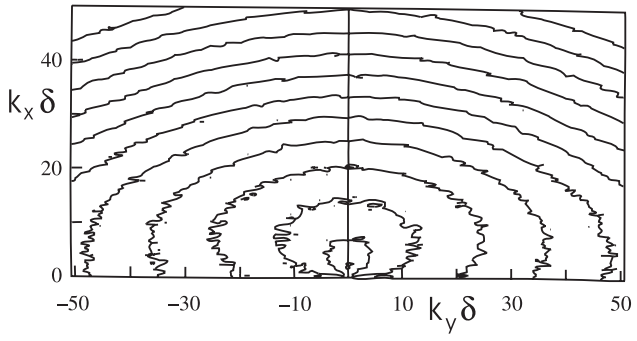

Fig. 10. Contour plots of the wavevector spectrum of the wall-pressure fluctuations $\phi(k_x,k_y)u_\tau/\tau_p^2\delta^2$ (12 levels in logarithmic sequence from 10^{-7} to $10^{-1.5}$ with a 0.5 increase in the exponents).

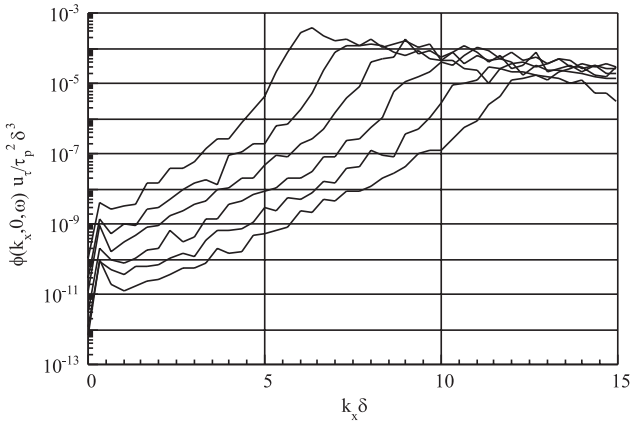

Fig. 11. Three-dimensional spectrum of the wall-pressure fluctuations $\phi(k_x,0,\omega)u_\tau/\tau_p^2\delta^3$ at small wavenumbers for several fixed frequencies ($\omega\delta/u_\tau = 103$ to 203 with increment of 20).

Frequency spectra (Fig. 13) contain some residual oscillations at high frequencies due to secondary zones in the averaging window. The existence of a ω^2 range at low frequencies is in agreement with the results of Manoha (1991).

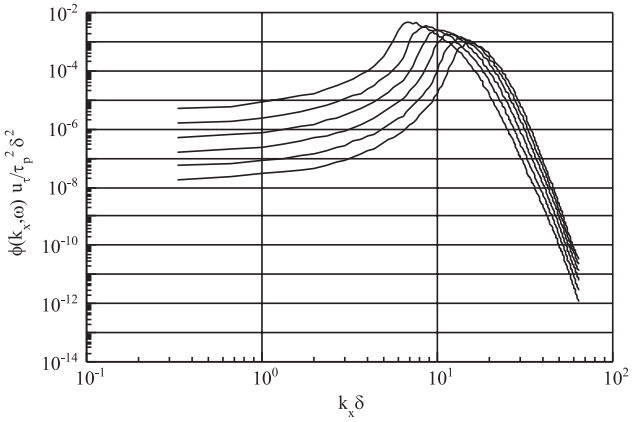

Fig. 12. wavenumber frequency spectrum of the wall-pressure fluctuations $\phi(k_x,\omega)u_\tau/\tau_p^2\delta^2$ for several fixed frequencies ($\omega\delta/u_\tau = 103$ to 203 with increment of 20).

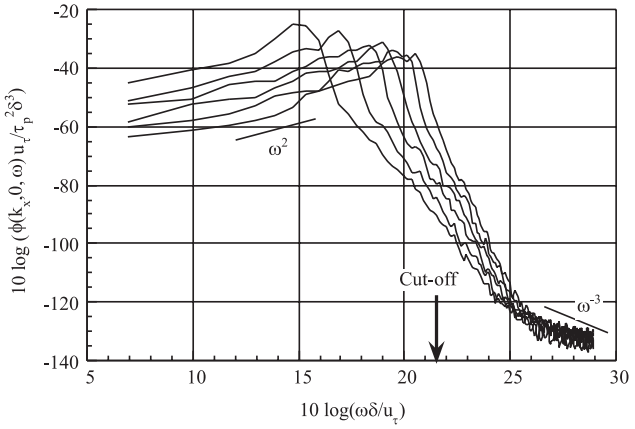

Fig. 13. Three-dimensional spectrum of the wall-pressure fluctuations $\phi(k_x,0,\omega)u_\tau/\tau_p^2\delta^3$ for several fixed wavenumbers ($k_x\delta = 2.0$ to 7.0 with increment of 1.0).

3.5. Convection velocities in spectral space

Convection velocities can be defined in several ways. In spectral space, the convection velocity U_c can be considered as a function of frequency and wavenumber and defined by

$$\frac{\partial}{\partial c_r}\phi\left(\frac{\omega}{c_r},\omega\right)=0 \quad \text{for } c_r = U_c(\omega), \tag{15}$$

where $c_r = -\omega/k_x$ denotes the phase velocity. Fig. 14 shows a good agreement with the various experimental results.

3.6. Root-mean-square of the wall-pressure fluctuations

Various results for the rms of the wall-pressure fluctuations, including the experimental data and direct numerical simulations in channel flow and boundary layers, are gathered in Fig. 15. The rms value of 1.9 obtained in the present calculations is significantly lower than the experimental results in boundary layers but seems to be in agreement with the channel flow data and in particular with the numerical DNS. Comparisons with the experimental data are indeed a tricky task

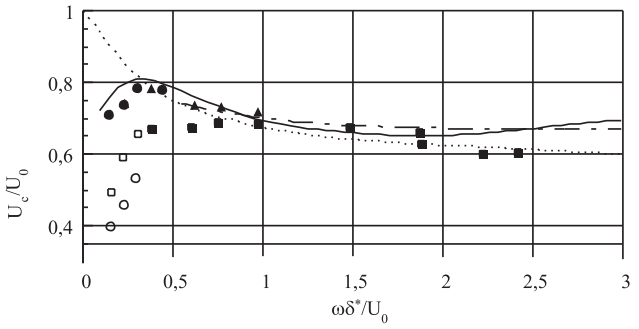

Fig. 14. Broad-band convection velocity as a function of the frequency. — Present calculation (LES); ..... (Bull, 1967, exp. (from Blake)); – · – · – (Willmarth and Wooldridge, 1965, exp. (from Blake)); Symbols (Blake, 1970, experiments).

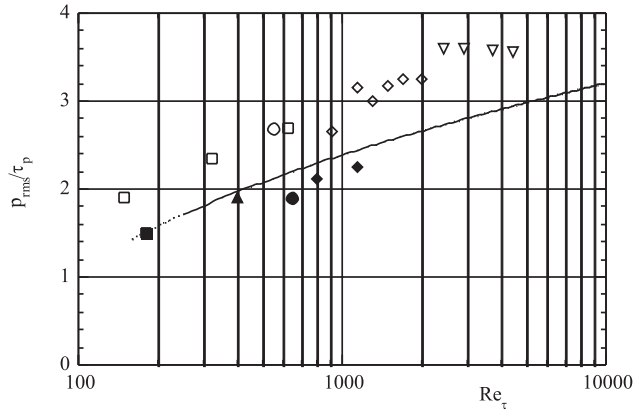

Fig. 15. Root-mean-square of pressure fluctuations versus Reynolds number. Black symbols: plane channel flow; light symbols: boundary layer. ● Present calculation (LES); ■ (Choi and Moin, 1990, DNS); ▲ (Kim, 1989, DNS); ◆ (Horne, 1989, exp.); □ (Spalart, 1988, DNS); ○ (Schewe, 1983, exp.); ◇ (Farabee and Casarella, 1991, exp.); ▽ (Blake, 1970, exp.); solid curve, law (17).

because it is difficult to clearly distinguish between the Reynolds number effects and transducer resolution limitations. At $Re_\tau = 400$ the DNS of Kim (1989) also gives a value of 1.9, suggesting that the present results are thus slightly underestimated since it is well established that the rms pressure increases with the Reynolds number (in the present calculation $Re_\tau = 640$).

Two main observations have thus to be emphasised: on the one hand, the rms of pressure fluctuations increases with the Reynolds number (cf. Panton and Linebarger, 1974); on the other hand, the rms of pressure fluctuations in a channel is lower than the one in a boundary layer at the same Reynolds number (this is even true at Reynolds numbers above 250 for which a very energetic ω^{-1} region is developing in the boundary layer as well as in the channel flow). This second point is clearly visible in Fig. 15 which includes two values of Reynolds numbers that are very close ($Re_\tau = 320$ and 400), Spalart (1988) obtains $p_{rms}/\tau_p = 2.35$ in the boundary layer while Kim obtains $p_{rms}/\tau_p = 1.9$ in the channel flow. As we have discussed before, the decrease of rms of pressure fluctuations in channel flow compared to the boundary layer can be explained by a difference in the spectral levels in the medium frequency range.

3.7. Cross-spectral features: coherence functions

In general, it is customary to define the cross-spectrum by the Fourier transform of the space-time correlations, which is a complex function (composed of a co-spectrum and a quadrature spectrum):

$$\phi(X, r_x, \omega) = C(X, r_x, \omega) - \mathrm{i}Q(X, r_x, \omega). \tag{16}$$

The coherence spectrum is then defined by

$$\Gamma(x, r_x, \omega) = \frac{|\phi(x, r_x, \omega)|}{\sqrt{\phi(X_1, \omega)\phi(X_2, \omega)}} \tag{17}$$

with $\phi(X, \omega)$ being the integrated frequency spectrum.

The angle is defined by

$$\theta = \tan^{-1}\left[Q(X, r_x, \omega)/C(X, r_x, \omega)\right] \tag{18}$$

A phase velocity can then be defined by

$$U_p(r_x, \omega) = \omega r_x/\theta. \tag{19}$$

The longitudinal coherence function is plotted in Fig. 16 as a function of the phase angle $\theta = \omega r_x/U_p$, for the different space intervals. It represents the decay of wall-pressure fluctuations in the convective process. It can be noticed that for high frequencies, there is a tendency for a similarity behaviour along a common unique curve, while at low frequencies there is important loss.

This similarity at high frequencies implies that all the pressure fluctuations decay with the same rate verifying

$$\theta(r_x, \omega) = k_x r_x = 2\pi r_x/\lambda \tag{20}$$

with λ being the wavelength of the fluctuations. Corcos (1963) in his model supposes that the longitudinal coherence function can be represented by an exponential law of the kind:

$$\Gamma(r_x, \omega) = \exp\left[-\gamma_1|\omega r_x/U_c|\right], \tag{21}$$

where γ_1 is an empirical constant. In the literature, this constant is usually supposed to take a value between 0.1 and 0.19. The value calculated in the present simulation is $\gamma_1 = 0.18$. The high value of this constant can be explained by the fact that the Reynolds number is moderate (the lower the Reynolds number, the faster the decay).

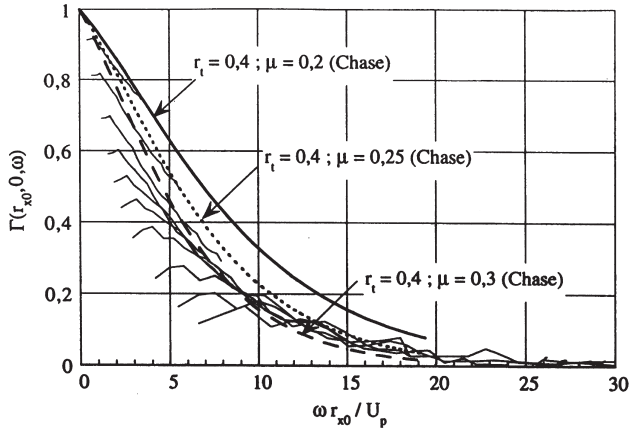

Fig. 16. Longitudinal coherence function of the wall-pressure field versus phase angle. — Present calculation (r_{x0}/δ is ranging from 0.025 to 0.375 with step values of 0.025).

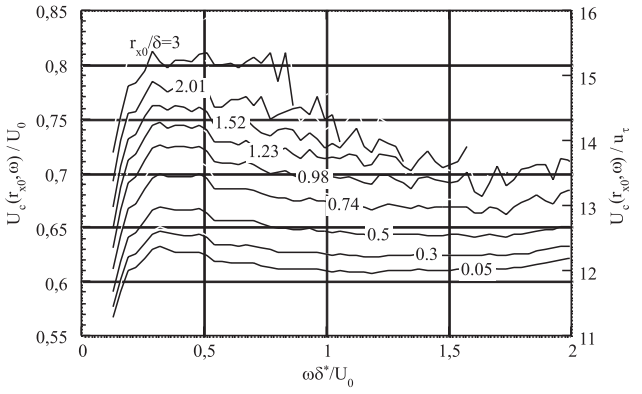

Fig. 17. Phase velocity as a function of frequency (r_{x0}/δ is ranging from 0.05 to 3.0).

3.8. Cross-spectral features: phase velocities

The phase velocity calculated from the angle of the longitudinal coherence function is presented in Fig. 17 as a function of frequency for different space intervals. The phase velocity distributions present a maximum value around $\omega\delta^*/U_0 \approx 0.3$ or $\omega\delta/u_\tau \approx 50$. This behaviour is in qualitative agreement with the known experimental data.

3.9. Space-time correlation and space correlation

The space-time correlation contours displayed in Fig. 18 clearly exhibit the convective crest in agreement with the experimental findings of Willmarth and Wooldridge (1965) and the DNS of Choi and Moin (1990). The individual space-time correlations plotted in Fig. 19 bring to light the location of the maxima of time correlation for different space intervals. The location of the maxima is in good agreement with the experimental data of Blake (1986).

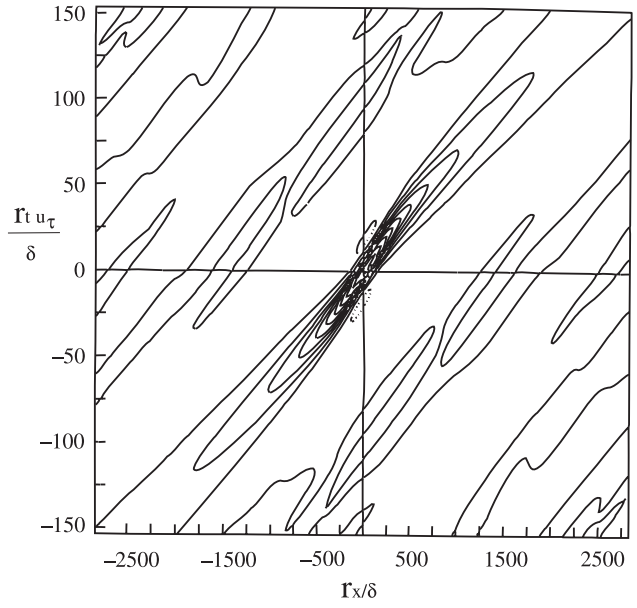

Fig. 18. Space-time isocorrelation levels of the wall-pressure field (10 levels from -0.1 to 0.9 with increment value of 0.1).

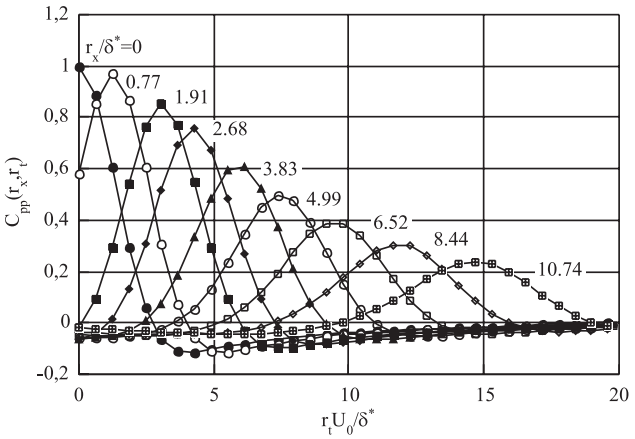

Fig. 19. Space-time correlations of the wall-pressure field as a function of time increment for different fixed space increments.

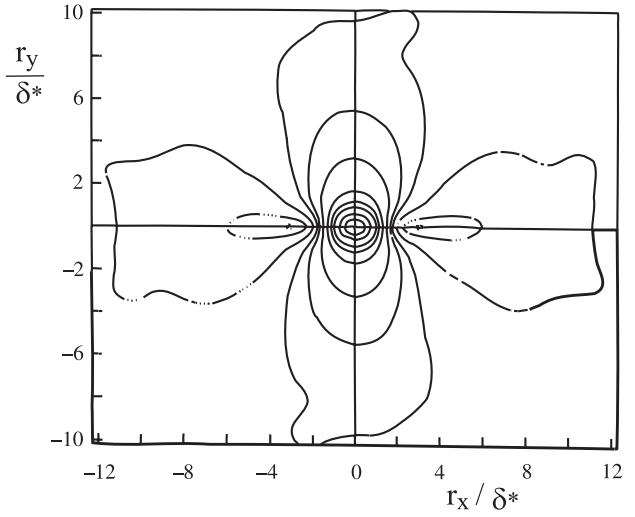

Fig. 20. Spatial correlation of the wall-pressure field in the longitudinal and transverse directions.

Contours of the spatial correlation, represented in Fig. 20, are clearly elongated in the transverse direction, in contrast with all other quantities and in particular the velocities.

3.10. Convection velocities in physical space

Convection velocities can be defined in physical space by the ratio r_x/r_t of the space and time intervals that maximize the space-time correlation $R(r_x, r_t)$. Fig. 21 shows the convection velocity profile as a function of the space interval for a fixed value of the time interval, confirming a very good agreement with the experimental data.

3.11. Comparisons with pressure spectra models

Corcos (1963) was the first author to devise an empirical model of the wall-pressure field. On the basis of measurements made by Willmarth, he supposes that the longitudinal and transverse coherence functions of wall pressure can be represented by an exponential law. This model implies that the pressure field is only dependent on the similarity variables. These similarity hypotheses are only valid in the high-

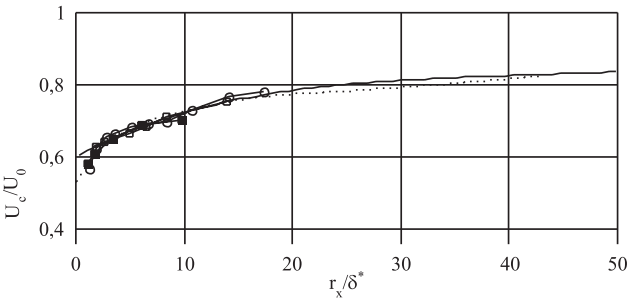

Fig. 21. Convection velocities in physical space as a function of the longitudinal r_x separation distance. —— Present calculation (LES); ..... (Bull, 1967, exp. (from Blake)); Symbols (Blake, 1970, experiments).

frequency domain. The Corcos model is able to predict correctly the convective properties of the pressure field but fails in the small wavenumber range giving overestimated levels.

Ffowcs Williams (1982) has proposed to modify this previous model in the small wavenumber range by taking into account the effect of compressibility. Extra numerical constants are introduced that are difficult to determine. For this reason, Hwang (see Manoha, 1991) proposed a simplified version of the model easier to handle.

Chase proposed a spectrum model applicable for a large interval of wavenumbers from small wavenumbers up to the convective zone by using a specific representation of the behaviour of each different source of pressure fluctuations. The model takes into account the two main contributions in the pressure fluctuations generation that are: the mean shear/turbulence interaction and the turbulence/turbulence interaction. The first Chase (1980) model has been later extended by a more general formulation by Chase (1987).

The Witting (1986) model is based on an explicit dipole representation of the near wall eddies. This mechanical description allows us to characterise the pressure spectrum for a large range of wavenumbers. These models are shortly recalled in the Appendix A.

Fig. 22 gives an example of the comparison of the present calculation with several models including the Corcos model in its original form (A1) and in its modified form (A3). The best parameter fit for the modified Corcos model is found to be:

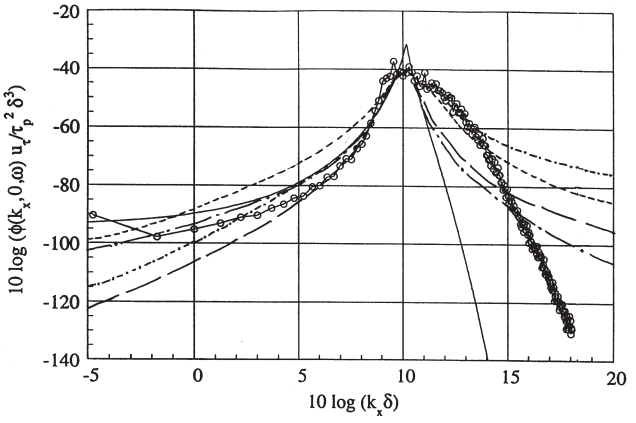

Fig. 22. Comparison of the wavenumber spectrum of the pressure field with analytical models (for $\omega\delta/u_\tau = 142.35$). —o— Present calculation; ..... (Corcos, 1963); – · – · – (Corcos, 1963, modified); – – – (Chase, 1987); — · — · — (Chase, 1987, modified); —— (Witting, 1986).

$b = 0.38$; $a_0 = 2$; $\alpha_1 = 0.19$; $\alpha_3 = 0.6$. The original Corcos model does give too high energy in the subconvective region. Also, the model assumes a ω^{-1} decay at high frequencies, while in the present calculation this behaviour is only prevailing in a very narrow frequency zone.

Using a similar practice as Hwang (see Manoha, 1991), this behaviour can be reproduced by introducing a correction factor, such that

$$\phi(k_x,k_y,\omega) = \phi_{\text{Corcos}}(k_x,k_y,\omega)\left(\frac{k_x U_c}{\omega}\right)^s. \tag{22}$$

This modified model produces a marked asymmetry in the convective peak. The best choice appears to be $s = 1.2$, a lower value than that proposed by Hwang, but this choice seems to be Reynolds number-dependent.

Fig. 22 also gives a comparison with the Chase models. The choice of numerical parameters are here: $b = 0.38$; $h = 2$; $C_M = 0.16$; $C_T = 10^{-3}$. In this case also, the modified model allows a better representation of the convective peak.

The Witting model is one of the few models taking into account the Reynolds number effects. Indeed the $z_{\min}/\delta^*$ parameter allows to cut more or less the spectrum at high frequencies, and by using a sufficiently high value for this constant it becomes possible to obtain a ω^{-1} slope up to $\omega\delta/u_\tau = 0.4Re_\tau$ corresponding to a good frequency behaviour.

The parameters used in Fig. 22 are $C = 7$, $z_{\max}/\delta^* = 8$ and $z_{\min}/\delta^* = 0.65$.

4. Effect of space-time perturbations on the wall-pressure fluctuations

The influence of space-time periodic perturbations is now studied by forcing a small amplitude sinusoidal normal velocity at the lower wall of the channel. The aim is to determine to what extent the pressure spectrum distributions are modified by wall perturbations. This kind of boundary condition is essentially different from a vibration of the plate, but it can probably give an idea of the order of magnitude of the effect.

4.1. Imposed perturbation

The normal velocity imposed at the lower wall is given by

$$w_{\text{wall}}(x,y) = A(t)\sin(\omega_1 x)\sin(\omega_2 y). \tag{23}$$

The perturbation is also sinusoidal in time $A(t) = A_0\sin(2\pi f t)$, with a given frequency f.

The wavelength of the perturbation is equal to $2\pi/\omega_1$ in the longitudinal direction, while in the present study ω_2 has been kept equal to zero (Dejoan et al., 1997).

The calculation has been made for a Reynolds number $Re_\tau = 640$, and Table 2 shows the numerical grid characteristics (the superscript "+" indicates the wall units). The grid resolution is the same as in the non-perturbed case, but the size of the domain is reduced by 2/3.

In the present simulation, the values of the parameters are fixed to

$$\begin{aligned} &A_0/u_\tau = 0.075, \quad f = 2u_\tau/\delta, \\ &\omega_1 = 0.5/\delta, \quad \omega_2 = 0, \quad \lambda_1 = 2\pi/\omega_1 = 4\pi\delta. \end{aligned} \tag{24}$$

The time step of the time integration is $\Delta t\, u_\tau/\delta = 4.10^{-4}$. The order of magnitude of the amplitude A_0 is chosen by reference to usual situations encountered in marine hydroacoustics. The wavelength λ_1 and the frequency f are determined in such a way that the large-scale range is excited (of the

Table 2
Characteristics of the computational domain in the perturbed case

N_x	N_y	N_z	L_x	L_y	L_z	h_x/δ	h_y/δ	h_z/δ	h_x^+	h_y^+	h_z^+
256	128	62	$4\pi\delta$	$\pi\delta$	2δ	0.049	0.025	1.38×10^{-3}–8.1×10^{-2}	31.4	15.71	0.88–51.84

order of the integral scale). A preliminary study made on a coarse mesh has shown that lower amplitudes have no appreciable effect at all on the numerical results. Low frequencies are difficult to reach because they would need very large integration times that would be prohibitive. One can also suppose that low frequencies are less interesting because a quasi-steady regime is expected to prevail. Besides, high frequencies are also of less interest because they cannot interfere with the energetic scales of turbulence.

4.2. Statistical treatment

Each turbulent quantity is split into three terms, as it is usual in pulsed flow studies. So, for an instantaneous Φ quantity, we write

$$\Phi = \bar{\Phi} + \tilde{\Phi} + \Phi' \tag{25}$$

and $\langle\Phi\rangle = \bar{\Phi} + \tilde{\Phi}$ represents the statistical mean obtained by phase average, Φ' the turbulent fluctuation and $\bar{\Phi}$ is the temporal mean value.

In practice, phase averages $\langle\Phi\rangle$ are operated in the y-direction (with periodic boundary conditions) and over the phase. All statistical treatments are made on purely turbulent components such as Φ'. The numerical simulation has been performed for a duration of six periods in which time a subset of 780 data points has been extracted. Every overlap window (Hanning window) is composed of two periods (i.e. 260 data points) and five overlays have been used on the whole signal. All other numerical aspects are identical to the method used in the non-perturbed case presented in the previous sections.

4.3. Spectra and correlations

Both the frequency spectra and wavenumber spectra undergo a slight increase at low frequencies and at low wavenumbers k_x. The other parts of the spectrum remain practically unchanged. It is also found that the k_y wavenumber spectra in the transverse direction are not modified in comparison with the non-perturbed case, probably because the imposed wall perturbation is indeed varying only in the longitudinal direction (because ω_2 has been kept equal to zero).

We found that the space-time isocorrelations are qualitatively almost identical to Fig. 18 for the non-perturbed case. However, the perturbed flow is found to display a wider distribution thus corresponding to a higher correlation in the fluctuations of pressure signal.

Modifications in the frequency-wavenumber spectra $\phi(k_x,\omega)$ and the wavevector spectra $\phi(k_x,k_y)$ are very slight and confirm the previous remarks (Viazzo and Schiestel, 1995).

4.4. One-point pressure statistics

Fig. 23 gives the pressure variance profiles near the lower wall as phase averages for different longitudinal locations and for different phase shifts. It appears that if the time mean values are only very slightly modified, the phase averages exhibit more variations. In particular, a maximum of variance is found (Fig. 23(a) and (c)) in the suction zone of the wall. Considering that these two figures correspond each to $A(0) = A(T/2) = 0$, and that the variance distributions are however different, it means that hysteresis effects are present.

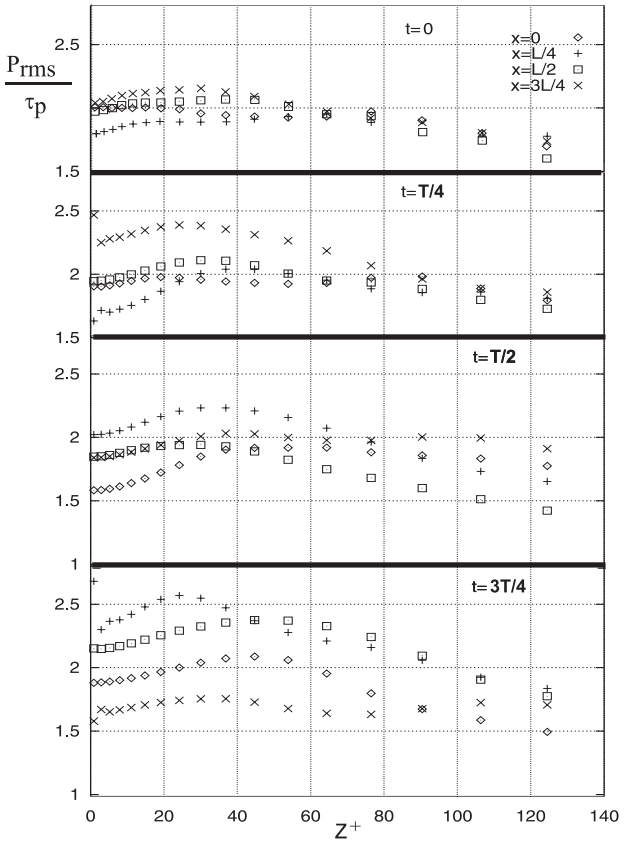

Fig. 23. Root-mean-square of pressure fluctuations on the lower wall in the perturbed case (time $t = 0, t = T/4, T = T/2, T = 3T/4$).

5. Concluding remarks

The large eddy simulation approach proved to be a useful tool for predicting the statistical properties of the turbulent wall-pressure field in channel flow, provided a sufficiently large computational domain is used for representing the large scales. Detailed information on the space-time correlations and spectra that are necessary for acoustical applications can be fairly well estimated from the numerical database. Comparisons between the various classical models for the pressure spectrum are in good general agreement with the results obtained from the calculation, while it is not really possible to infer the superiority of one of them. Indeed, all the models are practically in good agreement in the convective zone which contains most of the energy, but some discrepancies appear in the small wavenumber range. Some of the models which have been compared present interesting characteristics that are corroborated by the numerical simulation: the asymmetry of the convective peak (Hwang model), Reynolds number effects (Witting model). The effect of Reynolds number which is fairly low in the present LES has to be mentioned, considering that most of the classical models have been established for high Reynolds numbers. That is why the ω^{-1} zone prevails only on a very restricted region of the spectrum.

The effect of sinusoidal perturbations imposed on one wall of the channel is very weak, as far as the mean time values are considered. If one remarks that such a sinusoidal perturbation can more or less correspond to the order of magnitude of the effect of the preferred mode of vibration of the plate, even if the physical phenomenon is different, the present results may justify the usual hypothesis that vibrations of the plate do not influence the flow itself. However, a more detailed investigation using phase averages, like it is practised in pulsed flows, shows that the turbulent field is modified when frequencies of the perturbation interact with the characteristic frequencies of turbulence, and that some hysteresis effects exist.

Acknowledgements

The calculations have been carried on the CRAY C98 computers at the IDRIS in Paris which is gratefully acknowledged.

Appendix A

(1) Corcos (1963) model

$$\phi(k_x,k_y,\omega)=\frac{\gamma_1\gamma_2}{\pi^2}\left(\frac{\omega}{U_c}\right)^2\left\{\phi(\omega)\left[\left(k_x-\frac{\omega}{U_c}\right)^2+\frac{\gamma_1\omega}{U_c}\right]^{-1}\times\left[k_y+\left(\frac{\gamma_3\omega}{U_c}\right)^2\right]^{-1}\right\},\tag{A.1}$$

where γ_1, γ_3 are the numerical constants and U_c is the convection velocity.

(2) Ffowcs Williams (1982) model

$$\phi(k_x,k_y,\omega)=\rho^2U_c^3\delta^3\left(\frac{\omega\delta}{U_c}\right)\phi_0(\omega)A_0\left(1+\frac{k_xU_c}{\omega}\right)\times\left\{a_0\left(\frac{kU_c}{\omega}\right)^2+a_1M^2+a_2M^4\,\mathrm{Ln}\left(\frac{R}{\delta}\right)\boldsymbol{\delta}\left[\left(\frac{kU_c}{\omega}\right)^2-M^2\right]\right\},\tag{A.2}$$

where ϕ_0, A_0 and B_0 are the empirical functions, $\boldsymbol{\delta}$ the Dirac measure, M the Mach number and a_0, a_1 and a_2 are the empirical constants.

(3) Hwang model

$$\phi(k_x,k_y,\omega)=\phi_{\mathrm{Corcos}}(k_x,k_y,\omega)\left(\frac{k_xU_c}{\omega}\right)^2.\tag{A.3}$$

(4) Chase (1980, 1987) models

$$\phi(k_x,k_y,\omega)=\phi_M(k_x,k_y,\omega)+\phi_T(k_x,k_y,\omega),\tag{A.4}$$

$$\phi_T(k_x,k_y,\omega)=\rho^2u_\tau^3\left\{C_Tk^2\Big/(k^2+(b\delta)^{-2})^{\mu}\left[\frac{(\omega-U_ck_x)^2}{(hu_\tau)^2}+k^2+(b\delta)^{-2}\right]^{5/2-\mu}\right\},$$

$$\phi_M(k_x,k_y,\omega)=\rho^2u_\tau^3\frac{C_Mk_x^2}{\left[(\omega-U_ck_x)^2/(hu_\tau)^2+k^2+(b\delta)^{-2}\right]^{5/2}},$$

where $\mu=0$ gives the 1980s model and $0<\mu\leqslant1$ gives the 1987s model.

(5) Modified Corcos model by Chase

$$\phi(k_x,k_y,\omega)=a_0\rho^2u_\tau^4\left(\omega^2+(U_c/b\delta)^2\right)^{-1/2}\times\left[\left\{\pi^{-2}\alpha_1^3\alpha_3\left(\omega^2/U_c^2+(b\delta)^{-2}\right)k_x^2\right\}\Big/\times\left\{\left[(k_x-\omega/U_c)^2+\alpha_1^2\left(\omega^2/U_c^2+(b\delta)^{-2}\right)\right]^2\times\left[k_y^2+\alpha_3^2\left(\omega^2/U_c^2+(b\delta)^{-2}\right)\right]\right\}\right].\tag{A.5}$$

(6) Witting (1986) model

$$\phi(k_x,k_y,\omega)=p_{\mathrm{rms}}^2\frac{\delta^{*3}}{U_c}A\frac{\hat{\omega}}{\xi^5}\frac{8}{3}\int_{\xi_{\min}}^{\xi_{\max}}x^4\mathrm{e}^{-2x}\,\mathrm{d}x,\tag{A.6}$$

where

$$\xi=\hat{k}+C|\hat{\omega}-\hat{k}_x|,$$

$$\xi_{\max}=\xi z_{\max}/\delta^*,$$

$$\xi_{\min}=\xi z_{\min}/\delta^*,$$

$$\hat{k}_x=k_x\delta^*,\quad \hat{k}_y=k_y\delta^*,\quad \hat{k}=\sqrt{\hat{k}_y^2+\hat{k}_y^2},\quad \hat{\omega}=\omega\delta^*/U_c,$$

$$A=\frac{C}{\pi}\frac{1}{(1+2/3C^2)\,\mathrm{Ln}(z_{\max}/z_{\min})}.$$

References

Bally, P., 1989. Etude expérimentale des parties convective et à petits nombres d'onde des fluctuations de pression pariétale sous une couche limite turbulente en gradient de pression statique nul et positif. Thèse Université Aix-Marseille II.

Blake, W.K., 1986. Mechanics of Flow-Induced Sound and Vibration. Academic Press, London.

Blake, W.K., 1970. Turbulent boundary layer wall pressure fluctuations on smooth or rough walls. J. Fluid Mech. 44 (4), 637–660.

Bradshaw, P., 1967. Inactive motion and pressure fluctuations in turbulent boundary layers. J. Fluid Mech. 30, 241–258.

Bull, M.K., 1967. Wall pressure fluctuations associated with subsonic turbulent boundary layer flow. J. Fluid Mech. 28, 719–754.

Chase, D.M., 1980. Modeling the wavevector-frequency spectrum of turbulent boundary layer wall pressure. J. Sound Vib. 70, 29–67.

Chase, D.M., 1987. The character of the turbulent wall pressure at subconvective wavenumbers and a suggested comprehensive model. J. Sound Vib. 112 (2), 125–147.

Choi, H., Moin, P., 1990. On the space-time characteristics of wall-pressure fluctuations. Phys. Fluids A 2 (8), 1450–1460.

Comte-Bellot, G., 1963. Ecoulement turbulent entre deux parois parallèles. Publication Scientifique et Technique du Ministère de l'Armée de l'Air, 419.

Corcos, G.M., 1963. Resolution of pressure in turbulence. J. Acoust. Soc. Am. 35, 192–199.

Dejoan, A., Vedy, E., Schiestel, R., 1997. Large eddy simulation of perturbed turbulent wall flows. In: 11th Symposium on Turbulent Shear Flows, Grenoble, France. Proc. 3, 30.25–30.30.

Farabee, T.M., Casarella, M.J., 1991. Spectral features of wall pressure fluctuations beneath turbulent boundary layers. Phys. Fluids A 3 (10), 2410–2420.

Ffowcs Williams, J.E., 1982. Boundary layer pressures and the Corcos model, a development to incorporate low wave number constants. J. Fluid Mech. 125, 9–25.

Horne, M., 1989. Physical and computational investigation of the wall pressure fluctuations in a channel flow, Ph.D. Dissertation, Department of Mechanical Engineering, The Catholic University of America, 1989.

Kim, J., 1989. On the structure of pressure fluctuations in simulated turbulent channel flow. J. Fluid Mech. 205, 421–451.

Kraichnan, R.H., 1956a. Pressure field within homogeneous anisotropic turbuence. J. Acoust. Soc. Am. 28 (1), 64–72.

Kraichnan, R.H., 1956b. Pressure fluctuations in turbulent flow over a flat plate. J. Acoust. Soc. Am. 28 (3), 378–390.

Kwak, D., Reynolds, W.C., Ferziger, J.H., 1975. Three-dimensional time-dependent computation of turbulent flows, Department of Mechanical Engineering, Stanford University, California, Report TF-5.

Manoha, E., 1991. Wall pressure wavenumber-frequency spectrum beneath a turbulent boundary layer measured with transducer arrays calibrated with an acoustical method, ASME Winter Annual Meeting, Atlanta, GA, USA.

Moin, P., Kim, J., 1982. Numerical investigation of turbulent channel flow. J. Fluid Mech. 118, 341–377.

Monin, A.S., Yaglom, A.M., 1975. Statistical Fluid Mechanics II. MIT Press, Cambridge, MA.

Panton, R.L., Linebarger, J.H., 1974. Wall pressure spectra for equilibrium boundary layers. J. Fluid Mech. 65, 261–287.

Panton, R.L., Goldman, A.L., Lowery, R.L., Reischman, M.M., 1980. Low-frequency pressure fluctuations in axisymmetric turbulent boundary layers. J. Fluid Mech. 97 (2), 299–319.

Phillips, O.M., 1956. On the aerodynamic surface sound from a plane turbulent boundary layer. Proc. R. Soc. London A 234, 327–335.

Schewe, G., 1983. On the structure and evolution of wall pressure fluctuations associated with turbulent boundary layer flow. J. Fluid Mech. 134, 311–328.

Schiestel, R., Viazzo, S., 1995. A Hermitian–Fourier numerical method for solving the incompressible Navier–Stokes equations. Comput. Fluids 24 (6), 739–752.

Simpson, R.L., Ghodbane, M., McGrath, B.E., 1987. Surface pressure fluctuations in a separating turbulent boundary layer. J. Fluid Mech. 177, 167–186.

Schumann, U., 1975. Subgrid scale model for finite difference simulations of turbulent flows in plane channels and annuli. J. Comput. Phys. 18, 367–404.

Spalart, P.R., 1988. Direct simulation of a turbulent boundary layer up to $Re_\theta = 1410$. J. Fluid Mech. 187, 61–98.

Viazzo, S., 1993. Simulation de grandes structures turbulentes en canal plan et application à l'étude du champ de pression pariétale, Thèse Université Aix-Marseille II.

Viazzo, S., Schiestel, R., 1995. Simulations des grandes échelles turbulentes en canal à l'aide d'un schéma hermitien. Comptes Rendus de l'Académie des Sciences, t. 321, série II b, 225–232.

Willmarth, W.W., Wooldridge, C.E., 1965. Measurements of the fluctuating pressure at the wall beneath a thick turbulent boundary layer. J. Fluid Mech. 21, 107–109.

Witting, J.M., 1986. A spectral model of pressure fluctuations at a rigid wall bounding an incompressible fluid, based on turbulent structures in the boundary layer. Noise Control Eng. J. 26 (1), 28–43.